Monthly Notices of the ROYAL ASTRONOMICAL SOCIETY

MNRAS **497,** 956–968 (2020) doi:10.1093/mnras/staa1959
Advance Access publication 2020 July 8

Warm dust in high-z galaxies: origin and implications

L. Sommovigo,[1]★ A. Ferrara,[1,2] A. Pallottini,[1,3] S. Carniani,[1] S. Gallerani[1] and D. Decataldo[1]

[1]*Scuola Normale Superiore, Piazza dei Cavalieri 7, I-56126 Pisa, Italy*
[2]*Kavli Institute for the Physics and Mathematics of the Universe (WPI), University of Tokyo, Kashiwa 277-8583, Japan*
[3]*Centro Fermi, Museo Storico della Fisica e Centro Studi e Ricerche 'Enrico Fermi', Piazza del Viminale 1, I-00184 Rome, Italy*

Accepted 2020 June 19. Received 2020 June 18; in original form 2019 December 13

ABSTRACT

ALMA observations have revealed the presence of dust in galaxies in the Epoch of Reionization (EoR; redshift $z > 6$). However, the dust temperature, $T_{\rm d}$, remains unconstrained, and this introduces large uncertainties, particularly in the dust mass determinations. Using an analytical and physically motivated model, we show that dust in high-z, star-forming giant molecular clouds (GMCs), largely dominating the observed far-infrared luminosity, is warmer ($T_{\rm d} \gtrsim 60$ K) than locally. This is due to the more compact GMC structure induced by the higher gas pressure and turbulence characterizing early galaxies. The compactness also delays GMC dispersal by stellar feedback, thus ~ 40 per cent of the total UV radiation emitted by newly born stars remains obscured. A higher $T_{\rm d}$ has additional implications: it (a) reduces the tension between local and high-z IRX–β relation, and (b) alleviates the problem of the uncomfortably large dust masses deduced from observations of some EoR galaxies.

Key words: ISM: clouds – dust, extinction – galaxies: high-redshift.

1 INTRODUCTION

Astrophysical dust is a crucial component of the interstellar medium (ISM) of galaxies both in the local and high-redshift Universe (e.g. Weingartner & Draine 2001; Gallerani et al. 2010; Capak et al. 2011; Riechers et al. 2013; Weiß et al. 2013; Laporte et al. 2017). Dust scatters and absorbs UV and optical light emitted by newly born stars, and re-emits it at far-infrared (FIR) and millimetre wavelengths as thermal radiation. Therefore, dust strongly impacts the observed flux and detectability of galaxies at these wavelengths (Calzetti et al. 2000; Kriek & Conroy 2013), despite it typically only accounts for less than few percent of the total ISM mass (Draine & Li 2007).

Given the observed FIR spectra, spectral energy distribution (SED) fitting techniques ideally allow us to infer the dust temperature, dust mass, total infrared luminosity, and obscured star formation rate (SFR) of a galaxy (Walcher et al. 2011; Casey, Narayanan & Cooray 2014a). This is more common at $z < 5$, thanks to both Herschel coverage at FIR wavelengths, and (sub)mm coverage from ground-based facilities, such as SCUBA, the Atacama Large Millimeter Array (ALMA), and the Northern Extended Millimeter Array (NOEMA) (e.g. Walcher et al. 2011; Kirkpatrick et al. 2015).

For high-z galaxies ($z > 5$), deep FIR observations have only recently become possible thanks to the high sensitivity of millimetre interferometers such as ALMA and NOEMA (e.g. Capak et al. 2015; Willott et al. 2015; Bouwens et al. 2016; Barisic et al. 2017; Laporte et al. 2017; Bowler et al. 2018). Nevertheless, to date, ALMA observations put only loose constraints on the SED shape of 'normal' (i.e. main-sequence) galaxies in the Epoch of Reionization (EoR). This is because most of the current ALMA programmes have observed the dust continuum emission only in a single (or two, in a few cases) ALMA band (e.g. Bouwens et al. 2016; Barisic et al. 2017; Bowler et al. 2018; Laporte et al. 2019). As a consequence, SED-fitting techniques used at lower redshifts are not reliably applicable. Instead, given the broad-band fluxes in the available ALMA band(s), a 'dust temperature' must be assumed[1] together with a functional shape of the dust SED in order to extrapolate the integrated FIR luminosity, $L_{\rm FIR}$ (Capak et al. 2015; Bouwens et al. 2016; Barisic et al. 2017; Bowler et al. 2018). This SED sampling problem might be solved in the future thanks to proposed instruments such as SPICA (Spinoglio et al. 2017; Egami et al. 2018), featuring mid-infrared capabilities, and/or more extensive ALMA observations in other bands Faisst et al. (2020). For the moment, as a result of the uncertainties in the assumed dust temperature, the many derived properties of high-z galaxies are poorly constrained.

For instance, in the last years there has been tension regarding the surprisingly low infrared excess (IRX) of high-z galaxies, defined as IRX $\equiv L_{\rm FIR}/L_{\rm UV}$, where $L_{\rm UV}$ is the rest-frame luminosity at 1600 Å (e.g. Calzetti, Kinney & Storchi-Bergmann 1994; Calzetti 1997; Meurer, Heckman & Calzetti 1999). In particular, the relation between the IRX and the UV spectral slope β at $z > 5$ has been a matter of debate. This relation is particularly important since it is used to correct for dust obscuration in UV-selected galaxies at $z > 5$. Interestingly, high-z galaxies have been shown to have on average smaller IRX values with respect to local analogues, barred the relatively large scatter in the data (Casey et al. 2014b; Capak

[1]We underline here that the 'dust temperature' adopted for estimating $L_{\rm FIR}$ depends on the assumed dust SED functional shape, and does not necessarily reflect the physical dust temperature (e.g. Casey 2012; Casey et al. 2018; Liang et al. 2019).

★ E-mail: laura.sommovigo@sns.it

et al. 2015; Bouwens et al. 2016; Fudamoto et al. 2020). Warmer dust would imply a higher FIR luminosity and IRX parameter, which would largely reconcile tension between the IRX–β relationship of the local and the high-z galaxies (Bouwens et al. 2016; Faisst et al. 2017; Behrens et al. 2018).

Additionally, uncertainties in the dust temperature result in unreliable dust mass estimates. For instance, warmer dust can produce the same observed FIR flux without implying uncomfortably large dust mass, which are in tension with dust formation time-scale constraints (see e.g. Leśniewska & Michałowski 2019). This issue clearly emerges, for example, in the analysis of the galaxy MACS0416Y1 at redshift $z = 8.31$, for which Bakx et al. (2020) obtained an upper limit to the continuum flux at 160 μm (rest frame). Taken together with the previous continuum emission measurement at 90 μm Tamura et al. 2019), Bakx et al. (2020) conclude that the dust temperature is >80 K. As a consequence, the dust mass estimate is reduced by a 10-fold with respect to the value deduced by Tamura et al. (2019) (which corresponds to 3–8 $\times$ 10^6 $M_\odot$), obtained assuming $T_d = 40$–50 K (see Section 7.3 for a detailed discussion).

In this context, theoretical studies are a crucial complementary tool in order to interpret high-redshift observations. For instance, zoom-in simulations have been used to capture the internal properties and dynamics of galaxies in their cosmological environment, by consistently following the star formation history and feedback processes driving the chemical evolution of high-z galaxies (e.g. Pallottini et al. 2017a, b; Hopkins et al. 2018; Lupi et al. 2018; Rosdahl et al. 2018). These studies have identified some important differences between early and local galaxies. Pristine systems tend to have more compact sizes, higher specific SFR, and a more turbulent ISM than their local analogues, consistently with observations (e.g. Glazebrook 2009; González-López et al. 2014; Genzel et al. 2017).

Moreover, hydrodynamical simulations (Behrens et al. 2018; Arata et al. 2019; Liang et al. 2019; Ma et al. 2019) can be post-processed with physically rich radiative transfer computations to determine the relation between FIR emission properties and dust mass, temperature, geometry, and chemical composition. Behrens et al. (2018) pointed out that most of the FIR emission in early systems comes from a few massive, UV-opaque, star-forming complexes – in brief giant molecular clouds (GMCs) – while the UV flux mostly arises from a diffuse ISM component with relatively low optical depth. A spatial segregation of the FIR and UV emitting regions has been indeed observed at $z \sim 6$ (Faisst et al. 2017; Laporte et al. 2017; Bowler et al. 2018).

However, simulations themselves have some limitations due to the demanding computational times that the most detailed ones (in terms of considered physical processes, and resolution) require (Gordon et al. 2001; Baes et al. 2003; Bianchi 2008; Baes et al. 2011; Ceverino, Glover & Klessen 2017; Behrens et al. 2018; Liang et al. 2019; Ma et al. 2019; Bakx et al. 2020). In this sense, semi-analytical models, such as the one presented here, are complementary to simulations (Ferrara et al. 2017; Popping, Puglisi & Norman 2017). The aim of this work is to clarify the physical conditions and emission properties of dust in star-forming regions of EoR galaxies. Particularly, we focus on the dust within star-forming GMCs, since we expect that the emission from these regions has the strongest impact on the shape of the FIR SED. We refer to Ferrara et al. (2017) for a complementary treatment including the diffuse ISM.

The paper is organized as follows. In Section 2, we derive the main properties of GMCs and compare them with the most updated simulations. We select two prototypical GMCs as representative of the Milky Way (MW) and high-z galaxies population to examine the environmental dependence of their properties. In Section 3, we compute the effects of star formation on the GMC structure, develop a model for H II regions, and assess the cloud lifetime against dispersal due to radiative or mechanical processes. Section 4 contains the adopted dust model; in Section 5, we compute the dust temperature in GMCs including the effects of radiation pressure on the dust and gas distribution. In Section 6, the FIR GMC spectra are discussed, and compared with local observations and cosmological simulations. In Section 7, we discuss some important implications of our work; a summary (Section 8) concludes the paper.

2 GIANT MOLECULAR CLOUDS

We model GMCs as homogeneous spheres of densities ρ and radius R, characterized by a turbulent velocity with a 3D r.m.s. velocity dispersion σ and pressure p. We assume supersonic turbulence ($\sigma \gg c_s$, the sound speed of the gas). This simplification is supported by numerical simulation results showing that the ISM of high-z galaxies is highly turbulent (Pallottini et al. 2017b; Vallini et al. 2018). The density ρ can then be written as $\rho = p/\sigma^2$, neglecting the thermal pressure.

Assuming that GMCs have mass M, we introduce the virial parameter

$$\alpha_{\rm vir} = \frac{5\sigma^2 R}{3fGM}, \tag{1}$$

where f is a geometrical factor related to the cloud internal density profile. For spherical clouds with a radial density profile $\rho \propto r^{-\gamma}$, it is $f = (1 - \gamma/3)/(1-2\gamma/5)$. We assume $f = 1$ for our homogeneous cloud and $\alpha_{\rm vir} = 5/3$, which is consistent with local observations (Heyer et al. 2009) and simulations of GMCs (Grisdale et al. 2018).

The cloud mass, radius, and total hydrogen column density ($N_{\rm H}$) can be written as

$$M = \frac{1}{2}\frac{\sigma^4}{\sqrt{G^3 p}} \tag{2a}$$

$$R = \frac{1}{2}\frac{\sigma^2}{\sqrt{Gp}} \tag{2b}$$

$$N_{\rm H} = \frac{1}{2\mu m_{\rm p}}\sqrt{\frac{p}{G}}, \tag{2c}$$

where R is the Jeans length, $\mu = 2$ the mean molecular weight of the gas (we consider only H_2), and $m_{\rm p}$ the proton mass. The cloud gas number density can be expressed as $n = \rho/\mu m_{\rm p}$. Relations among the different quantities that enter in our calculations can be visualized in Fig. 1, where we also report the normalized σ-distribution in GMCs found in zoom-in simulations of a typical, simulated high-z galaxy from Leung et al. (2019) and Pallottini et al. (2019), Freesia. A comparison between the Milky Way (MW) and Freesia is summarized in Table 1.

We note that the r.m.s. dispersion retrieved from this simulation (for further details see Leung et al. 2019,[2] and also Kohandel et al., in preparation) spans a range $1 \lesssim \sigma_{\rm kms} \lesssim 30$, where $\sigma_{\rm kms} = \sigma/({\rm km\,s^{-1}})$, and has a median value $\sigma_{\rm kms} = 15.76$, which is on average higher than what expected from MW-like galaxies at low redshift ($\sigma_{\rm kms} \sim 5$, see observations by e.g. Larson 1981; Rosolowsky & Blitz 2005;

[2]Data for σ from the simulation are retrieved as a H_2 mass weighted PDF on a cell by cell basis. For the first moment of the distribution, there are almost no difference with respect to the extraction of data on a cloud by cloud basis, as shown in Leung et al. (2019).

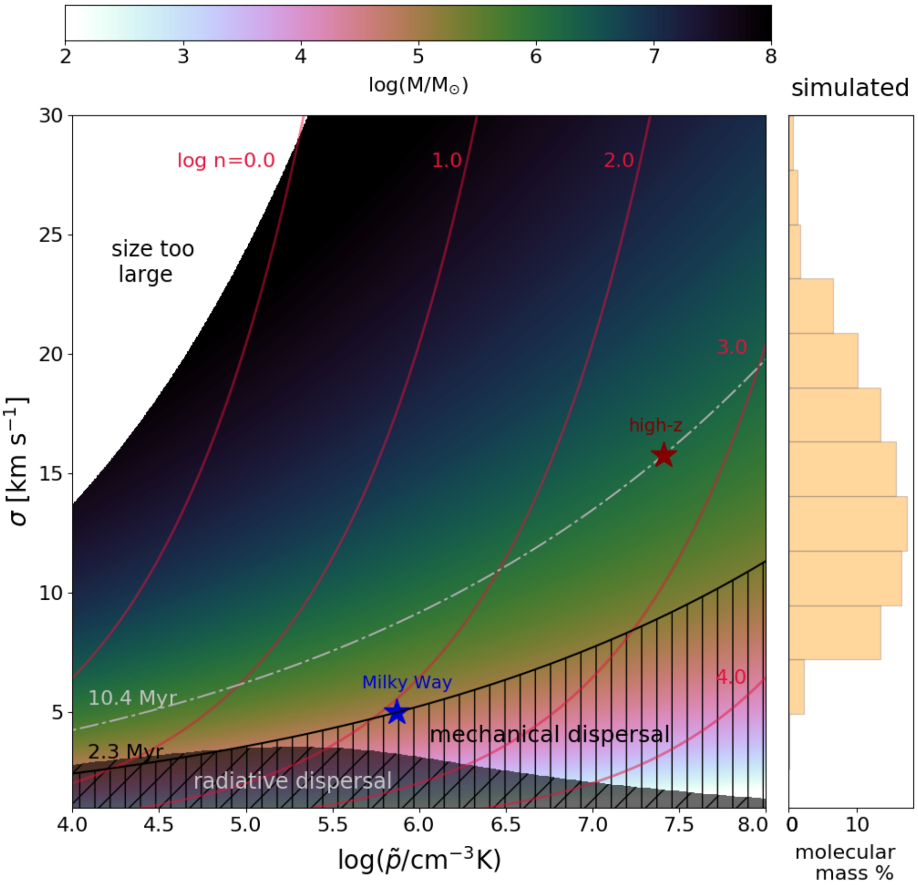

Figure 1. Overview of GMC properties: phase-space diagram of pressure versus dispersion for molecular clouds with masses between 10^2 and 10^8 $M_\odot$. The white region corresponds to clouds that have a size larger than 1 kpc. Red lines indicate those clouds with number density $\log n = 0.0, 1.0, 2.0, 3.0$, and 4.0. The grey region shows the clouds dispersed by the expansion of the H II regions (radiative dispersal) before 4 Myr, while the hatched region indicates those clouds dispersed by either SN explosion or stellar winds (mechanical dispersal) before 2.3 Myr. The blue and brown star marks correspond to a typical GMC in the Milky Way (MW, $\sigma = 5$ km s^{-1}, $\tilde{p} = 10^{5.87}$ cm^{-3} K; Semenov et al. 2018; Decataldo, in preparation) and high-z galaxies ($\sigma = 15.76$ km s^{-1}, $\tilde{p} = 10^{7.41}$ cm^{-3} K; Pallottini et al. 2019), respectively. The grey dashed line represents the mechanical dispersal time for typical high-z GMCs ($t_{\rm d,Myr} = 10.4$) and the black one for the MW-like clouds ($t_{\rm d,Myr} = 2.3$). In the right vertical panel, we report the normalized distribution of the σ in GMCs found in a zoom-in simulation of a typical high-z galaxy (Freesia, see Pallottini et al. 2019).

Table 1. Properties of the Milky Way and simulated high-z galaxy, Freesia. Data taken from (1) Licquia & Newman (2015), Xue et al. (2008), and (2) Pallottini et al. (2019).

Galaxy	$M_{\rm halo}$ (10^{11} M$_\odot$)	M_* (10^9 M$_\odot$)	SFR (M$_\odot$ yr^{-1})	z	Ref.
MW	10^{+3}_{-2}	60.8 ± 11.4	1.65 ± 0.19	0	(1)
Freesia	0.59	4.2	11.5 ± 1.8	8	(2)

Heyer et al. 2009, and simulations by e.g. Grisdale et al. 2018; Semenov, Kravtsov & Gnedin 2018). Derived GMC pressures in high-z clouds are comparable to those found in the Galactic centre, i.e. $6 \lesssim \log \tilde{p} \lesssim 8$, where $\tilde{p} = p/k_{\rm B}$ cm^{-3} K, with $k_{\rm B}$ being the Boltzmann constant. Simulations (e.g. Pallottini et al. 2019), in agreement with observations (Shibuya et al. 2014), also find that the effective radii of galaxies at $z = 6$ are <1 kpc. In order to exclude unphysically large GMC sizes in our model, we only consider the $p-\sigma$ parameter space satisfying $R < 1$ kpc (i.e. we cut off the white region in Fig. 1), corresponding to $\sigma_{\rm kms} < (p/k_{\rm B})^{1/4}$. With these assumptions, our model includes GMC masses in the range $2 \leq \log(M/{\rm M}_\odot) \leq 8$.

3 STAR FORMATION AND H II REGIONS

To determine the dust temperature in GMCs, we need to estimate the star formation rate (SFR), and the associated flux of UV photons heating the dust grains. In addition, it is important to study the effects of H II regions both on GMC dispersal and density structure as a result of the dynamical effects occurring during the H II region evolution. We consider all the stars to be located in the centre of our GMCs.

The SFR can be estimated by assuming a Schmidt–Kennicutt (Schmidt 1959; Kennicutt et al. 1998) relation,

$$\mathrm{SFR} = \epsilon_{\rm ff}\frac{M}{t_{\rm ff}} = \frac{1}{2}\epsilon_{\rm ff}\frac{\sigma^3}{G} = 10^{-5.9}\sigma^3_{\rm kms}\,{\rm M}_\odot{\rm yr}^{-1}, \quad (3)$$

where we use the relations given in equation (2) for the cloud mass; $t_{\rm ff} \propto 1/\sqrt{G\rho}$ is the cloud free-fall time, and $\epsilon_{\rm ff} \approx 0.01$ is the amount of gas converted in stars within $t_{\rm ff}$. For the latter value we consider the average computed by Krumholz & Tan (2007), who analysed a variety of GMCs observed within the MW. Note that in our model the SFR does not depend on pressure, but only on σ.

In the absence of feedback impairing the star forming ability of the cloud, equation (3) implies a gas depletion time for the GMC

equal to $t_{\rm dep} \equiv M/{\rm SFR}$, or[3]

$$t_{\rm dep,Myr} = \frac{t_{\rm ff}}{\epsilon_{\rm ff}} = 10.5\,\sigma_{\rm kms}\,\tilde{p}_8^{-1/2}\,. \quad (4)$$

Massive stars produce ionizing ($h\nu > 13.6$ eV) photons which create an H II region around the star-forming site. The size of the ionized bubble is set by recombination-ionization equilibrium, and it is equal to the Strömgren radius $R_{\rm S}$:

$$R_{\rm S} = (3\dot{N}_{\rm i}/4\pi n_{\rm e}^2\alpha_{\rm B})^{1/3}\,, \quad (5)$$

which is reached after approximately a recombination time,

$$t_{\rm r} = (n_{\rm e}\alpha_{\rm B})^{-1}. \quad (6)$$

In the previous expressions, $\dot{N}_{\rm i}$ is the ionizing photon rate, $n_{\rm e}$ is the electron number density, and $\alpha_{\rm B}$ ($T = 10^4$ K) $= 2.6 \times 10^{-13}$ cm^3 s^{-1} the case B hydrogen recombination coefficient. As for gas densities $n_{\rm e} > 1\,{\rm cm}^{-3}$, $t_{\rm r} < 2 \times 10^4$ yr, which is much shorter than the evolutionary time-scale of the massive stars driving the H II region, we can safely assume that the Strömgren sphere forms instantaneously.

We consider that star formation proceeds in a continuous mode, according to a Salpeter single power-law initial mass function (IMF) with stellar mass range 1–100 M$_\odot$. We assume a metallicity $Z = 0.5\,{\rm Z}_\odot$. We then use the population synthesis code STARBURST99 (Leitherer et al. 1999) and the Geneva tracks (Schaerer et al. 1993) to derive the ionizing photon rate conversion, $\dot{N}_{\rm i} = \eta_i\,{\rm SFR/M}_\odot\,{\rm yr}^{-1}$, with $\eta_{\rm i} = 10^{53.4}$. With these assumptions we find

$$R_{\rm S} = 0.14\,\sigma^{7/3}\,p^{-2/3} = 3.7 \times 10^{-3}\,\sigma_{\rm kms}^{7/3}\,\tilde{p}_8^{-2/3}\ {\rm pc}. \quad (7)$$

Therefore, the H II region size decreases for increasing GMC pressure, shrinking to (sub-)pc scales when $\tilde{p}_8 \gtrsim 1$ (for $\sigma_{\rm kms} \sim 15$, namely the one of our high-z cloud).

The overpressurized, ionized region begins to expand into the surrounding gas after a sound crossing time, $t_{\rm c} = R_{\rm s}/c_{\rm i}$, where $c_{\rm i} \approx 10\,{\rm km\,s}^{-1}$ is the sound speed in the ionized gas. Stated differently, the ionization front (IF) makes a transition from R-type to D-type. It is straightforward to show that the condition $t_{\rm r} < t_{\rm c}$ is equivalent to $c_{\rm i} < n_{\rm e}\alpha_{\rm B}(3\dot{N}_{\rm i}/4\pi n_{\rm e}^2\alpha_{\rm B})^{1/3} \sim 43\ n^{1/3}\sigma_{\rm kms}\,{\rm km\,s}^{-1}$. Hence, we conclude that an R-type phase always precedes the D-type, under realistic conditions.

3.1 GMC dispersal

As H II regions expand, they inject kinetic energy in the GMC and might ultimately destroy the cloud by dispersing it. In addition to radiation, massive stars produce stellar winds, and ultimately supernova explosions. In the following we provide separate estimates for these effects in terms of their ability to disrupt the cloud and quench star formation. The timescale on which GMC dispersal occurs is crucial to predict the FIR dust luminosity, as will be discussed in Section 6.

3.1.1 Dispersal by H II regions

The expansion of the H II region, formed around newly born stars can lead to the dispersal of the cloud. This occurs via two distinct processes: (a) if the Strömgren radius exceeds the GMC radius, $R_{\rm S} > R$, the IF is density-bounded and the cloud undergoes essentially free-expansion in the lower pressure diffuse ISM, rapidly dispersing. The time-scale for the dispersal is approximately equal to the H II region sound crossing time $t_{\rm c} = R_{\rm S}/c_{\rm i}$; (b) if $R_{\rm S} < R$, the GMC can still be dispersed during the subsequent D-type expansion of the front, starting at $t_{\rm c}$.

By using equation (5), we first determine the conditions for which $R_{\rm S}$ exceeds the GMC radius, which is given by equation (2). We find that $R_{\rm S}$ is always smaller than the GMC radius for our assumed values of p and σ, as also reported by recent numerical simulations (Decataldo et al., in preparation). In fact, the condition $R_{\rm S} > R$:

$$\frac{R_{\rm S}}{R} = \frac{0.28\sigma^{7/3}/p^{2/3}}{\sigma^2/\sqrt{Gp}} > 1 \quad (8)$$

implies $n \ll 1\,{\rm cm}^{-3}$, corresponding to a cloud radius > kpc for fixed σ and p, i.e. exceeding the size of a typical galaxy at $z \approx 6$ (Shibuya et al. 2014).

Once the IF reaches $R_{\rm S}$, it makes a transition to a D-type front, in which the warm, ionized gas starts to expand, driving a shock into the surrounding neutral gas. To describe this process we follow the approach by Raga, Cantó & Rodríguez (2012). Assuming that (i) the shock is isothermal, (ii) the gas in the ionized region is uniform and in photoionization equilibrium, we can write the velocity of the IF at radius r as

$$\frac{1}{c_{\rm i}}\frac{{\rm d}r}{{\rm d}t} = \left(\frac{R_{\rm S}}{r}\right)^{3/4} - C\left(\frac{r}{R_{\rm S}}\right)^{3/4}, \quad (9)$$

where $C = (c_{\rm s}^2 + \sigma^2)/(c_{\rm i}^2 + \sigma^2)$ and $c_{\rm i}, c_{\rm s}$ are the sound speeds in ionized and neutral gas, respectively. Note that when $C = 0$ the solution by Dyson & Williams (1980) is recovered, and the H II region expands forever. With the boundary condition $r(t = 0) = R_{\rm S}$, equation (9) can be integrated analytically to obtain:

$$t' = \frac{1}{3C^{7/6}}[q(y) - q(1)] \quad (10a)$$

with $y = r/R_{\rm S}$, $t' = t\sqrt{c_{\rm i}^2 + \sigma^2}/R_{\rm S}$, and

$$q = -12\,C^{1/6}y^{1/4} + 2\sqrt{3}\arctan\left(\frac{\sqrt{3}\,C^{1/6}y^{1/4}}{1 - C^{1/3}y^{1/2}}\right) + \ln\left[\frac{(C^{1/3}y^{1/2} + C^{1/6}y^{1/4} + 1)(C^{1/6}y^{1/4} + 1)^2}{(C^{1/3}y^{1/2} - C^{1/6}y^{1/4} + 1)(C^{1/6}y^{1/4} - 1)^2}\right]. \quad (10b)$$

We now determine the stalling radius ($r_{\rm e}$) where the H II region expansion stops. The surviving clouds are those for which $r_{\rm e} < R$. Those not fulfilling this condition are (radiatively) dispersed over the time-scale $t'(r_{\rm e}/R_{\rm S})$ given by equation (10a). In Fig. 1, we identify GMCs with $t < 4$ Myr as the black hatched region. From the above analysis, we conclude that H II regions can only disperse relatively small, $M \leq 10^5$ M$_\odot$, weakly turbulent ($\sigma < 5\,{\rm km\,s}^{-1}$) clouds.

3.1.2 Dispersal by stellar winds and supernovae

Supernova (SN) explosions and stellar winds can disperse GMCs by accelerating gas to speeds exceeding the cloud escape velocity, $v_{\rm e}$. The number of supernovae produced by a given SFR at time t can be written as

$$N_{\rm SN}(t) = \Theta(t - t_{\rm SN})\nu_{\rm SN}{\rm SFR}\,t = 0.02\,\sigma_{\rm kms}^3\,t_{\rm Myr}\Theta(t - t_{\rm SN}), \quad (11)$$

where $\nu_{\rm SN} = (53\,{\rm M}_\odot)^{-1}$ is the number of SNe per solar mass of stars formed (Ferrara & Tolstoy 2000); the Heaviside function, $\Theta(t - t_{\rm SN})$, accounts for the mass-dependent delay between the onset of star formation and the SN explosion. We consider as a lower limit $t_{\rm SN} \sim 3$ Myr, which roughly corresponds to the lifetime of a 100 M$_\odot$ star (Schaerer & de Koter 1997), i.e. the largest mass in our IMF

[3]In this paper, we adopt the notation $Y_x = Y/10^x$

range. The energy released in kinetic form is then

$$E_{\rm SN}(t) = f_{\rm SN} E_0 N_{\rm SN}(t) = 2 \times 10^{48} \sigma_{\rm kms}^3 \, t_{\rm Myr} \Theta(t - t_{\rm SN}) \ \text{erg}. \quad (12)$$

We have assumed a kinetic-to-total energy efficiency $f_{\rm SN} \approx 0.1$ and a standard SN explosion energy of $E_0 = 10^{51}$ erg.

Before the SN explosion, a large amount of kinetic energy is also produced by stellar winds of massive stars,

$$E_{\rm w}(t) \simeq \frac{1}{3} E_{\rm SN} = 0.67 \times 10^{48} \sigma_{\rm kms}^3 \, t_{\rm Myr}, \quad (13)$$

where the ratio of 1/3 with respect to the SN explosion energy is taken from STARBURST99. The total mechanical energy is thus $E = E_{\rm SN} + E_{\rm w}$.

Using equation (2), the escape velocity of GMCs can be written as a function of σ as

$$v_{\rm e}^2 = \frac{2GM}{R} = 2\sigma^2 \, . \quad (14)$$

For the dispersal condition, we require that the kinetic energy is sufficient to accelerate the GMC gas mass to $v_{\rm e}$, i.e. $E \geq 0.5 \, M v_{\rm e}^2$. This condition defines a dispersal time $t_{\rm d}$, at which the cloud becomes unbound, and its gas returned to the diffuse phase. Using the above relations, we find

$$t_{\rm d,Myr} = \frac{t_{\rm d',Myr}}{\Theta(t_{\rm d',Myr} - t_{\rm SN,Myr}) + 1/3}, \quad (15)$$

where $t_{\rm d',Myr} = 1.94 \times 10^{-3} \sigma_{\rm kms}^3 \tilde{p}_8^{\ -1/2}$ would be the dispersal time assuming that SNe explode at $t_{\rm SN} = 0$. Thus, for the expected pressure in high-z galaxies ($\tilde{p} \simeq 3 \times 10^7$), GMCs with $\sigma_{\rm kms} \leq 15.76$ are dispersed in $\leq$10.4 Myr, while in the MW ($\tilde{p} \simeq 7 \times 10^5$) typical GMCs with $\sigma_{\rm kms} \leq 5$ are dispersed in $\approx$2.3 Myr. However, MW clouds can last for 17 Myr if we consider $\sigma_{\rm kms} \simeq 10$, i.e. for clouds with $M \sim 10^6 \, {\rm M}_\odot$ at the typical MW pressure. Our estimates are consistent with the recent cosmological zoom-in simulations of MW like galaxies by Benincasa et al. (2019). The authors measure the lifetimes of GMCs with masses above $\geq 10^5 \, {\rm M}_\odot$, finding average values below 7 Myr, with less than 1 per cent of clouds living longer than 20 Myr.

Before dispersal at time $t_{\rm d}$ (equation 15), dust in the GMC efficiently reprocesses the UV light of the stars into FIR emission. When the GMC is finally dispersed, the dust is ejected into the diffuse ISM on much larger scales, thus drastically decreasing its UV optical depth and quenching the FIR emission.

The fraction of GMC gas converted into stars ($f_* = M_*/M$) before dispersal can be derived by combining equations (4) and (15):

$$f_* = \frac{t_{\rm d}}{t_{\rm dep}} = \frac{1.8 \times 10^{-4} \sigma_{\rm kms}^2}{\Theta(t_{\rm d',Myr} - t_{\rm SN,Myr}) + 1/3}. \quad (16)$$

Thus, f_* vary from about 1.4 per cent for an MW-like cloud to 3.2 per cent for GMCs in high-z galaxies. This is yet another consequence of the higher turbulence level predicted for these systems. Since the GMC mass fraction converted into stars is low, we assume that the cloud density does not change with time due to star formation activity. We note that these are lower limits for the amount of stars formed, since we are considering the average free-fall time, neglecting the likely presence of local density inhomogeneities ('clumps', see e.g. Semenov et al. 2018). These structures may contribute significantly to star formation on very short time-scales since $t_{\rm ff} \propto \rho^{-1/2}$.

The above estimates can be seen as a rough approximation as some unwarranted assumptions have been made. First, equation (8) neglects radiative losses which are likely to occur during the blastwave evolution. Secondly, off-centre SNe might induce blisters which are not described by our simple geometry. Finally, the stochastic sampling of the IMF might result in values of $\nu_{\rm SN}$ which are different from the average one assumed here. In spite of these simplifications, equation (15) provides some useful guidance for the problem at hand, although we leave a more refined treatment to future work.

4 DUST MODEL

Following Weingartner & Draine (2001, herafter WD01), we model dust grains as constituted by a mixture of silicate and carbonaceous grains with a relative mass ratio $\approx$11:1 (see also Draine 2003). Grains are assumed to be spherical with radii in the range 10^{-3} μm $< a <$ 1 μm and with a size distribution given by WD01:

$$\frac{{\rm d}N^j}{{\rm d}a} \frac{1}{N_{\rm H}} = \frac{C_{\rm s}}{a} \left(\frac{a}{a_{\rm t,s}} \right)^{\alpha_{\rm s}} F(a, \beta_{\rm s}, a_{\rm t,s}) \, G(a, a_{\rm t,s}, a_{\rm c,s}) \, , \quad (17a)$$

where $C_{\rm s}, a_{\rm t,\,s}, a_{\rm c,\,s}, \alpha_{\rm s}$, and $\beta_{\rm s}$ are five parameters used to fit the observed extinction curves. In particular, we adopt extinction curve appropriate for the MW with $R_V = A_V/(A_B - A_V) = 3.1$, where A_B and A_V are the extinctions measured in the B (4400 Å) and V (5500 Å) spectral bands, respectively. In general, the Small Magellanic Cloud (SMC) is considered a fair local analogue for high-z galaxies because of its low metallicity. Nevertheless, there is no conclusive evidence that high-z dust should be SMC-like (e.g. Gallerani et al. 2010; Stratta, Gallerani & Maiolino 2011; Popping et al. 2017; Behrens et al. 2018; Bowler et al. 2018). For this reason, and to allow a direct comparison with local GMCs, we adopt an MW-like dust grain-size distribution and extinction curve. Moreover, we present results only for silicate grains since the contribution of carbonaceous grains is found to be negligible. We neglect the effect of coagulation and grain growth by accretion of gas phase metals occurring in dense environments, which might result in larger grains.

Under these assumptions, the functions $F(a, \beta_{\rm s}, a_{\rm t,\,s})$ and $G(a, a_{\rm t,\,s}, a_{\rm c,\,s})$ take the following form:

$$F = \begin{cases} 1 + \beta_{\rm s} \left(\frac{a}{a_{\rm t}} \right) & \beta_{\rm s} \geq 0 \\ \left[1 - \beta_{\rm s} \left(\frac{a}{a_{\rm t}} \right) \right]^{-1} & \beta_{\rm s} < 0 \end{cases}, \quad (17b)$$

$$G = \begin{cases} 1 & 3.5 \, \text{Å} < a < a_{\rm t,s} \\ e^{-[(a - a_{\rm t,s})/a_{\rm c,s}]^3} & a > a_{\rm t,s} \end{cases}. \quad (17c)$$

4.1 Radiation pressure in dusty H II regions

So far we have considered H II regions only in relation to their eventual dispersal of the GMCs. However, H II regions can also modify the dust and gas spatial distribution. For instance, radiation pressure from the internal sources, drags both dust and gas outwards (more or less efficiently depending on the strength of the radiation field), resulting in lower central densities. We now intend to modify our previous assumption of a uniform GMC gas/dust density profile by taking into account this effect. We follow the approach by Draine (2011), who assumes that the dust-to-gas ratio remains constant throughout evolution. This is equivalent to assuming that dust is well coupled to the gas, so that the radiation pressure acting on the dust directly determines the gas motion. This assumption is valid once that grains approach their terminal velocities (i.e. negligible acceleration). For gas densities $n > 10 \, {\rm cm}^{-3}$, and grain sizes in the range 10^{-3} μm $\leq a \leq 1$ μm, the time needed for grains to approach their terminal velocity – see equation 28 in Draine (2011), is a few

tens of years.[4] This is much shorter that the time-scales of interest here. So we conclude that grains can be safely assumed to be perfectly coupled to the gas.

We can then assume that the gas is in dynamical equilibrium, so that the force per unit volume from radiation pressure is balanced by the pressure gradient:

$$n\sigma_{\rm d}\frac{[L_{\rm n}{\rm e}^{-\tau}+L_{\rm i}\phi(r)]}{4\pi r^2 c}+\alpha_{\rm B}n^2\frac{\langle h\nu_{\rm i}\rangle}{c}-\frac{{\rm d}p}{{\rm d}r}=0, \tag{18a}$$

where $\sigma_{\rm d}$ the dust scattering and absorption cross-section per H nucleus averaged over the radiation field. $L_{\rm i}\phi(r)$ is the power in ionising photons ($h\nu_{\rm i}\geq 13.6$ eV) crossing a sphere of radius r, and $L_{\rm n}$ the one in non-ionizing photons (the central cluster UV luminosity is then equal to $L_{\rm n}+L_{\rm i}=L_{\rm UV}$). The function $\phi(r)$ and the dust absorption optical depth at the distance r (integrated over wavelength) $\tau(r)$ are determined by the differential equations:

$$\frac{{\rm d}\phi}{{\rm d}r}=-\frac{1}{\dot{N}_{\rm i}}\alpha_{\rm B}n^2 4\pi r^2-n\sigma_{\rm d}\phi, \tag{18b}$$

$$\frac{{\rm d}\tau}{{\rm d}r}=n\sigma_{\rm d}, \tag{18c}$$

with boundary conditions $\phi(0)=1$, and $\tau(0)=0$. Following the computation by Draine (2011), we numerically solve the system equations (18), fixing the pressure at the edge of the H II region, p, and $\dot{N}_{\rm i}$ to the corresponding values for the MW and high-z clouds.

The resulting[5] density profile $n(r)/n$, normalized to our homogeneous Jeans cloud density n, is shown in the upper panel of Fig. 3 for the high-z GMC. The (normalized) dust number density drops almost to zero for distances $\log x<-1.2$, and reaches $\simeq$3 at the Strömgren radius $R_{\rm S}$; outside the H II region the dust profile remains unaffected with respect to the uniform cloud case.

5 DUST TEMPERATURE

We now compute the dust temperature, $T_{\rm d}$, by balancing the dust photoheating rate,[6] $\dot{E}_+$, with the emission rate, $\dot{E}_-$. To this aim, we consider GMCs to be constituted by a series of concentric shells of dust and gas of radius $r=xR$, with fixed dust-to-gas ratio $D=0.01$. We then compute the temperature of a dust grain located in the shell at radius x, $T_{\rm d}(x,a)$, for different values of the grain size in the range 10^{-3} μm $<a<1$ μm. We adopt the internal radiation field provided by newly formed stars, $F_{\rm int}$, as the only UV radiation source. For the photoheating rate we get

$$\dot{E}_+=\int_{100\,\text{Å}}^{4000\,\text{Å}}\pi a^2 Q_{\rm abs}(\lambda,a)(1-{\rm e}^{-\tau_{\rm shell}})F_{\rm int}\,{\rm d}\lambda\,, \tag{19a}$$

$$F_{\rm int}=\frac{L_\lambda}{\pi(xR)^2}{\rm e}^{-\tau_\lambda}\,. \tag{19b}$$

The integral runs over the range 100 Å $<\lambda<$ 4000 Å since the UV flux out of this range contributes negligibly to grain heating in actively star-forming systems (Buat & Xu 1996). L_λ is the specific luminosity of the central cluster; using the SFR of our clouds (equation 3) we can write $L_{1500\text{Å}}=\eta_{1500\text{Å}}$ SFR and compute $\eta_{1500\text{Å}}$ using STARBURST99 (see Section 3 for the detailed assumptions). We find that $\eta_{1500\text{Å}}$ increases with the cloud lifetime, ranging from $10^{41.8}$ erg s^{-1}/M$_\odot$ yr^{-1} at 0.4 Myr of the cloud age, to $10^{43.1}$ erg s^{-1}/M$_\odot$ yr^{-1} at 10 Myr. The dust optical depth can be written as

$$\tau_\lambda=[\tau_\lambda]_0^R=\int_0^R n(r)\,{\rm d}r\int_{a_{\rm min}}^{a_{\rm max}}\pi a^2\,Q_{\rm abs}(\lambda,a)\,\frac{{\rm d}N}{{\rm d}a}(a)\,{\rm d}a\,. \tag{20}$$

Within a shell at radius r, and width 2dr, the optical depth is $\tau_{\rm shell}=[\tau_\lambda]_{r-{\rm d}r}^{r+{\rm d}r}$. d$N$/d$a$ is the grain size distribution given in equation (17), and $n(r)$ is the number density of the cloud, which is either uniform, or is computed via equation (18a) when taking into account the effect of radiation pressure.

The grain radiates energy at a rate given by

$$\dot{E}_-=4\pi\int_0^\infty\frac{4}{3}\pi a^3\delta_g B_\lambda(T_{\rm d})k_\lambda\,{\rm d}\lambda\,, \tag{21}$$

where B_λ is the Planck function and $k_\lambda(\lambda)$ the opacity per unit mass, which can be well approximated by a power law (for $\lambda>20$ μm) as in Draine (2003):

$$k_\lambda(\lambda)=k_{\rm abs}\left(\frac{\lambda}{\rm cm}\right)^{-\beta_{\rm d}} \tag{22}$$

the constant of proportionality in the MW extinction curve corresponds to $k_{\rm abs}=2.47\times10^{-3}$ cm^2 g^{-1}. Estimates of the power slope found in literature span the range $1\leq\beta_{\rm d}\leq2.5$ (e.g. Hildebrand 1983; Dunne et al. 2000; Dupac et al. 2003; Désert et al. 2008; Paradis, Bernard & Mény 2009; Paradis et al. 2010; Planck Collaboration XIX 2011a; Planck Collaboration XXV 2011b); here we adopt $\beta_{\rm d}=2$ as in Draine (2003). The equilibrium temperature[7] (e.g. Guhathakurta & Draine 1989; Draine & Li 2001). We neglect this effect in the paper, although we recognize that it might influence the observed emission under certain conditions. $T_{\rm d}(a,\beta,\Sigma_\lambda)$ can be then obtained by imposing $\dot{E}_+=\dot{E}_-$. Furthermore, we take into account the effect of the cosmic microwave background (CMB) acting as a thermal bath. We always correct the dust temperature (Da Cunha et al. 2013):

$$T_{\rm d}'=\{T_{\rm d}^{4+\beta_{\rm d}}+T_0^{4+\beta_{\rm d}}[(1+z)^{4+\beta_{\rm d}}-1]\}^{1/(4+\beta_{\rm d})}, \tag{23}$$

where $T_0=2.73$ K is the CMB temperature at $z=0$.

In Fig. 2, we show the results for $T_{\rm d}$ with/without the effects of radiation pressure on the dust density, for the typical grain radius $a=0.1$ μm. We compare dust temperatures for the prototypical MW and high-z GMC (blue and brown star in Fig. 1, respectively) at 0.4 Myr of stellar age, i.e. well before stellar feedback effects start to play a role. In the following, we analyse separately the results for uniform clouds, and the case including radiation pressure due to UV radiation.

5.1 Uniform cloud

In the left-hand panel of 2, we show that in the central region of uniform clouds ($\log x<-1$), dust is warmer by $\Delta T_{\rm d}\sim50$ K in high-z GMCs with respect to MW ones. The higher pressure of high-z GMCs results in larger N_H and τ values; radiation is more efficiently absorbed in the vicinity of the source, and therefore dust becomes

[4]More precisely, for the largest (slowest) grains in the two clouds we find $\tau_{\rm drag,\,MW}=43$ yr, and $\tau_{\rm drag,hz}=11$ yr.

[5]The above density profiles refer to a steady-state solution of the equations. Hence we have to ensure that the time-scale to reach such configuration is shorter than, for instance, the lifetime of massive stars. We compute the grain velocity due to radiation pressure, $v(r)$, by solving the momentum equation, $(L_{\rm UV}/4\pi r^2 c)\pi a^2 Q_{\rm abs}=m_{\rm g}v({\rm d}v/{\rm d}r)$, where $m_{\rm g}=(4\pi/3)\delta_g a^3$ is the mass of a grain of bulk density is $\delta_g\approx3$ gcm^{-3}. We estimate the transient time-scale as $\Delta t\approx R_{\rm S}/v(R_{\rm S})$, finding $\Delta t\ll1$ Myr. Hence, we can safely assume that the steady-state solution is instantaneously reached.

[6]We neglect collisional heating.

[7]Very small grains might undergo stochastic temperature fluctuations.

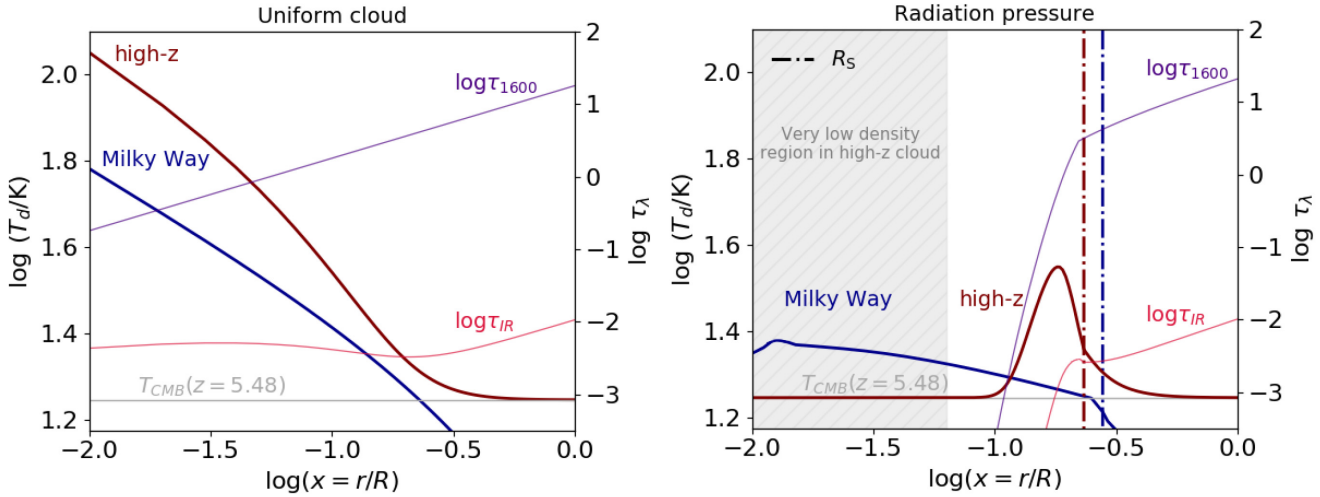

Figure 2. Dust temperature versus normalized distance from the centre of the cloud for typical grains with radius $a = 0.1$ μm. *Left-hand panel*: Case of a uniform GMC in which radiation pressure effects have been neglected. Blue and brown lines show the dust temperature profiles for an MW-like and high-z GMC, respectively. The properties of the two GMCs are the same of those marked as blue and brown stars in Fig. 1, and the stellar age is 0.4 Myr. The thin lines show respectively the values of the optical depth at 1600 Å (purple) impinging on dust grains at various distances from the centre of the cloud, and at the optical depth corresponding to the IR peak wavelength of emission $\lambda_{\rm peak}$ (red, see text) for the high-z GMC. *Right-hand panel*: as the left-hand panel, but the model takes into account the radiation pressure. The dashed dotted lines represent the location of the boundary of the H II region in the MW and high-z like cloud.

warmer.[8] To show this more quantitatively, we have plotted in Fig. 2 the optical depth $\tau_{1600\text{Å}}$ as a function of x. The dust mass heated by the internal source is essentially that contained within a radius, $r_{\rm d}$, such that $\tau_{1600\text{Å}}(r_{\rm d}) = 1$. For clouds with higher p, $r_{\rm d}$ decreases accordingly because of the higher column density (see equation 2), resulting in higher dust temperatures. This finding provides the physical basis to interpret the simulation results by Behrens et al. (2018). The authors, in fact, noticed that the galaxy regions with the highest dust temperature, which contribute to most of the FIR radiation, are optically thick.

Differences between early and local GMCs are also seen in the external layers ($\log x \gtrsim -0.5$). Due to the absorption of the UV radiation within the cloud, and in the absence of an external radiation field (such as the interstellar radiation field), $T_{\rm d}$ drops at the surface of the cloud down to the CMB temperature. The CMB acts as a thermal bath, setting a temperature floor for dust around 20 K at $z \gtrsim 6$ (see equation 23). This effect is sub-dominant in the central regions of the GMC, where dust reaches higher temperatures $T_{\rm d} \gg T_{\rm CMB}$. In Fig. 2, we computed the CMB correction for $z = 5.48$, i.e. the mean redshift of the Capak et al. (2015) sample.

We can understand these results in simple physical terms. Let us assume that the amount of dust heated by the internal radiation field is that contained within $r_{\rm d}$, the distance at which the dust optical depth is $\tau_{1600\text{Å}} \approx 1$. For a gas of solar metallicity ($Z = Z_\odot$) and dust-to-gas ratio $\mathcal{D} = \mathcal{D}_\odot = 0.01$, the condition $\tau_{1600\text{Å}} = 1$ is reached for a column density $N_1 = 1.4 \times 10^{21}\,{\rm cm}^{-2}$. By using equation (2), we find that the dust content within $r_{\rm d}$ is

$$M_{\rm d}(r_{\rm d}) = \mathcal{D}(\mu m_{\rm p})^3 N_1^3 \frac{\sigma^4}{p^2}. \tag{24}$$

As the UV light is completely absorbed by dust within $r_{\rm d}$ and re-emitted FIR wavelengths, we can write $L_{\rm FIR} \sim L_{1500\text{Å}} = 10^{2.9}\sigma_{\rm kms}^3 {\rm L}_\odot$. We can finally derive the dust temperature adapting to our dust model the formula from Dayal, Hirashita & Ferrara (2010),

$$T_{\rm d} = 3.24 \left(\frac{L_{\rm FIR}/{\rm L}_\odot}{M_{\rm d}/{\rm M}_\odot}\right)^{1/6} {\rm K} = 122\ \tilde{p}_8^{1/3}\sigma_{\rm kms}^{-1/6}\,{\rm K}. \tag{25}$$

This result shows that star-forming GMCs at higher pressure contain hotter dust. For example, for a pressure $p/k_{\rm B} = 10^{7.41}\,{\rm erg\,cm^{-3}\,K}$, and $\sigma_{\rm kms} = 15.76$ (typical of high-z simulated galaxies, Pallottini et al. 2019), we find $T_{\rm d} \sim 50\,{\rm K}$, in good agreement with the numerical result in Fig. 2. Although velocity dispersion modifies the dust temperature as well, its effect is less relevant than pressure. As already mentioned, $T_{\rm d}$ is virtually independent on SFR: as $\sigma \propto {\rm SFR}^{1/3}$, from equation (25) we deduce $T_{\rm d} \propto {\rm SFR}^{-1/18}$. Hence pressure is the primary factor controlling dust temperature. Thus, the physical explanation for the higher $T_{\rm d}$ in highly pressure environments is related to the limited amount of dust required to block the UV radiation. Dust located outside $r_{\rm d}$ cools to the CMB temperature as the flux from the stars is largely blocked.

So far we have assumed that the GMC is optically thin with respect to the FIR radiation. We motivate such choice by showing in Fig. 2 the optical depth $\tau_{\rm IR}$ at the peak wavelength of emission, computed from Wien's law: $\lambda_{\rm peak}T_{\rm d}(x) = 0.29\,{\rm cm\,K}$. We find that $\tau_{\rm IR} \ll 1$, i.e. dust is optically thin with respect to its FIR emission, even at this very high densities. Indeed, we can understand this by considering the optical depth at 100 μm from Draine (2003): $\tau_{100\ \mu{\rm m}}/N_{\rm H} = 5.07 \times 10^{-25}$, hence[9] in order to have $\tau_{100\mu{\rm m}} = 1$, $N_{\rm H} = 1.9 \times 10^{24}\,{\rm cm}^{-2}$. Using equation (2), we can compute the pressure needed to reach such value in our GMCs and we find $\tilde{p}_8 = 64$ which is outside the considered range. If these high pressures were to be reached, dust might become optically thick to FIR emission as well (see e.g. Conley et al. 2011; da Cunha et al. 2015).

[8] Although the higher SFR in the high-z cloud results in a larger $F_{\rm int}$, this does not imply a higher $T_{\rm d}$. We show below (equation 25) that the dust temperature in the GMC is virtually independent of the SFR.

[9] As a reference, the column density at the surface of our typical high-z cloud is $N_H = 3.7 \times 10^{22}\,{\rm cm}^{-2}$.

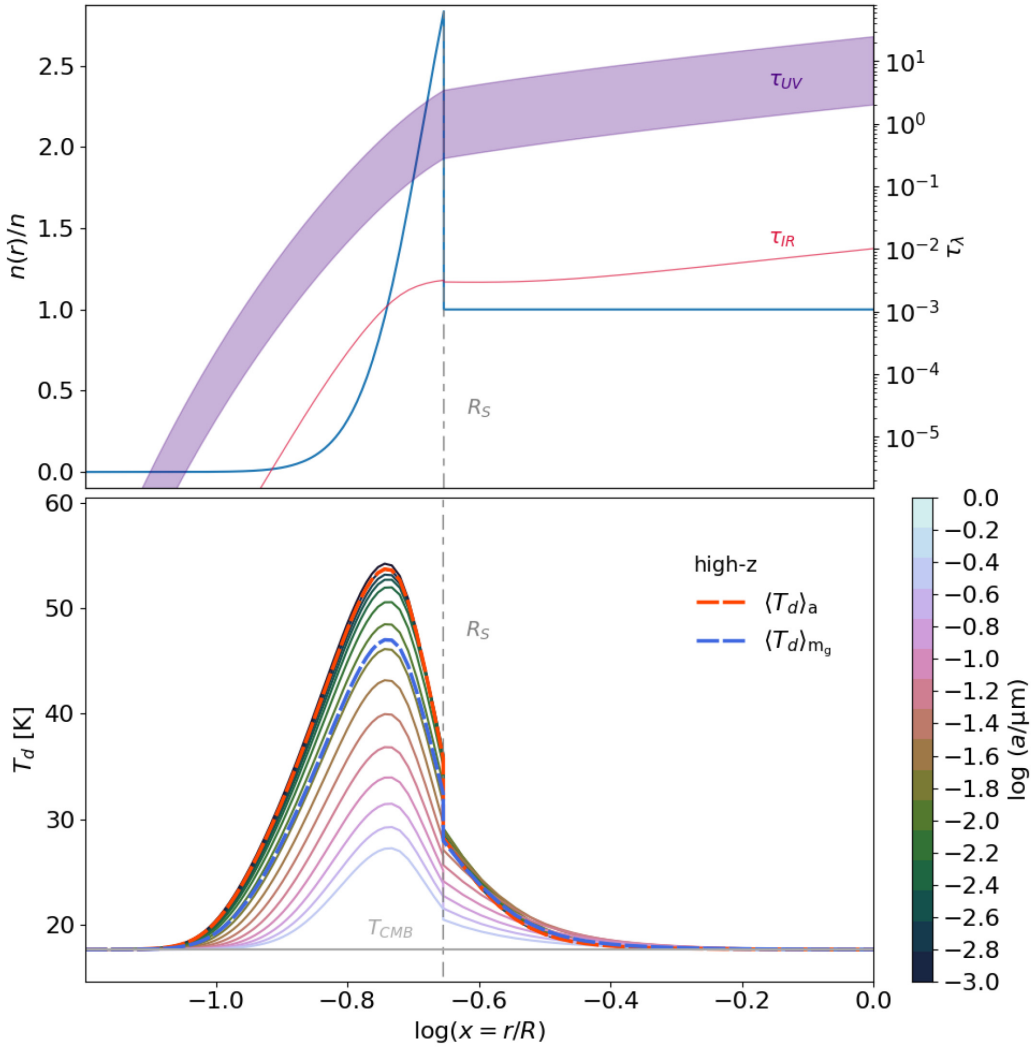

Figure 3. *Upper panel*: Dust density modified by the radiation pressure in the high-z GMC as a function of the normalized distance x from the centre. We also show the dust optical depth to UV radiation in the wavelength range 1500 Å $< \lambda <$ 3100 Å (purple shaded region, computed via equation 20), along with the dust IR optical depth (red solid line) at the peak emission wavelength. *Bottom*: Grain temperature for the high-z GMC as a function of radial distance from the centre and for different grain radii, colour-coded in the colourbar. The dashed line shows the size-averaged temperature, $\langle T_{\rm d} \rangle_a$. We consider a cluster stellar age 0.4 Myr.

5.2 Radiation pressure-modified density profile

Next, we consider dust temperature variations associated with the density redistribution induced by radiation pressure on dust described in Section 4.1. The obtained profiles of the dust temperature as a function of the distance are shown in the right-hand panel of Fig. 2. By comparing with the uniform cloud (left-hand panel), we see that the inclusion of radiation pressure decreases $T_{\rm d}$: for the high-z (MW) cloud $T_{\rm d}$ spans the range 17–40 K (2.73–25 K). The lower $T_{\rm d}$ in both cases is associated with the fact that dust is pushed at larger distances from the UV source where the flux is more geometrically diluted. We note that the resulting central region devoid of dust is much wider in the high-z GMC, where it extends up to $\log x = -1.2$ (see the grey hatched region). In the MW cloud this region is much smaller, $\log x \sim -3$. This is due to the larger UV luminosity resulting from the higher SFR, in turn associated with larger dispersion in the high-z GMC (SFR $\propto \sigma^3$, see equation 3). In both cases (high-z and MW clouds), the external layers are unaffected by the presence of the internal sources since the emitted radiation has already been absorbed within the cloud. Hence, no appreciable differences with respect to the uniform density case are found at large distances (in the absence of the external interstellar radiation field).

The dust temperature depends also on grain size, a, as shown in Fig. 3 in the case of the high-z cloud. We can isolate the terms related to the grain size in the photoheating and emission rates (equations 19b and 21), and find that $T_{\rm d} \propto [Q_{\rm abs}(\lambda, a)/a]^{1/6}$. The dependence of $T_{\rm d}$ on wavelength and grain radius is non-monotonic. Blueward of $\lambda = 1500$ Å smaller grains are more efficiently heated; at longer wavelengths 2000 Å $< \lambda <$ 3500 Å, intermediate grains with $a \sim 0.1$ μm have the highest $Q_{\rm abs}$ value. This has a noticeable effect on the dust grains temperatures at different radii in the GMC.

While within the H II region, the photoheating rate is dominated by short-wavelength UV radiation with $\lambda <$ 2000 Å, radiation with longer wavelengths ($\lambda \gtrsim$ 3000 Å) takes over in the external neutral layers. As a result, near the centre of the cloud ($\log x < -0.6$), the small grains, $a \sim 10^{-3}$ μm, are the hottest, reaching $T_{\rm d} > 50$ K. At the GMC surface, instead, intermediate size grains, $a \sim 0.1$ μm, attain the highest temperatures. These trends are clearly visible in the bottom panel of Fig. 3, where we also show the size-averaged temperature

$\langle T_{\rm d}\rangle_a$ and grain mass-averaged temperature $\langle T_{\rm d}\rangle_{\rm m_g}$ (averaged over $\mathrm{d}N/\mathrm{d}a \times 4\pi a^2 \mathrm{d}a$). At the surface of the cloud, independently of the grain size, the dust temperature converges to the CMB temperature due to the very high optical depth (see the purple shaded region in fig. 3 for the dependence of the grain size-averaged UV optical depth on the distance from the centre of the cloud).

We pause here for a remark. We considered the same continuous SFR described in Section 3 also in the radiation pressure modified density profile treatment. This is clearly an approximation, since the reduction in the central density of the cloud (shown in the upper panel of Fig. 3) actually affects the SFR, which is proportional to gas density. However, star formation is distributed all over the cloud, and not just in its centre (as shown also by recent fully resolved simulations, see Decataldo, in preparation). Therefore, the average SFR over the whole cloud will not necessarily change considerably, despite the local density drop. Although this approximation over the SFR has been introduced, we prefer to include radiation pressure in our models, since we have shown that it alters considerably our predictions on dust temperatures. Moreover, we underline that our main goal is to give a lower limit for the dust temperature in GMCs, and to show how this lower bound evolves from low to high-z. The radiation pressure case gives a lower temperature value with respect to the homogeneous case, and yet a higher $T_{\rm d}$ with respect to what so far assumed at high-z.

5.2.1 *Mass- and luminosity-weighted dust temperature*

From the above results we can compute the mass-weighted, $\langle T_{\rm d}\rangle_{\rm M}$, and luminosity-weighted, $\langle T_{\rm d}\rangle_{\rm L}$, dust temperature as a function the age of the stellar cluster accounting for the associated evolution of the UV luminosity (taken from STARBURST99 with the usual assumptions on the SFR and metallicity, see Section 3). We compute $T_{\rm d}$ in the time interval $0-t_{\rm d,Myr}$, where $t_{\rm d,Myr}$ is the GMC lifetime against dispersal caused by feedback processes (Section 3.1). As usual, in Fig. 4, we compare high-z and MW GMCs.

For the high-z cloud, most of the dust mass is in thermal equilibrium with the CMB, $\langle T_{\rm d}\rangle_{\rm M}^{\rm hi\text{-}z} \sim T_{\rm CMB}$. However, a small fraction of the dust located near the UV source is much hotter, and contributes strongly to the luminosity-weighted temperature. Indeed, we find $\langle T_{\rm d}\rangle_{\rm L}^{\rm hi\text{-}z} \sim 60\,{\rm K} \gg \langle T_{\rm d}\rangle_{\rm M}^{\rm hi\text{-}z}$ at 10 Myr of the central cluster stellar age. The luminosity-weighted temperature is of particular importance as it represents a good proxy for the dust temperature that would be inferred from the SED fitting of the source. Neglecting the effects of radiation pressure, would lead to even higher temperatures, $\langle T_{\rm d}\rangle_{\rm L}^{\rm hi\text{-}z} \sim 100$ K. This is because more dust would be found in the proximity of the source (at $\log x < -1$), as already discussed (see Section 5.2). The MW GMC is instead much colder, with $\langle T_{\rm d}\rangle_{\rm M}^{\rm MW} \leq 15$ K and $\langle T_{\rm d}\rangle_{\rm L}^{\rm MW} < 30$ K. This is because at $z = 0$ (i) the CMB temperature sets a much lower floor for $T_{\rm d}$, and (ii) the more diffuse structure of the cloud results in a less efficient dust heating (see Section 5.1). We will return to this point in the following Section.

6 INFRARED EMISSION

We predict the infrared luminosity of our star-forming GMCs by using the above grain mass-averaged temperature $\langle T_{\rm d}\rangle_{\rm m_g}$ (blue dashed line in Fig. 3), and weighting the contribution of each shell by its dust mass, $m_{\rm d,shell}$:

$$L_\lambda^i = \frac{8\pi hc^2}{\lambda^5}\frac{k_\lambda}{M_{\rm d}}\int_0^1 \frac{m_{\rm d,shell}(x)}{\exp(hc/k_{\rm B}\langle T_{\rm d}\rangle_{\rm m_g}\lambda)-1}\,\mathrm{d}x. \tag{26}$$

The comparison between the high-z and MW cloud is shown in Fig. 5 at the stellar age of 0.4 Myr. As expected, the IR emission from the high-z cloud is ∼30 times stronger due to its higher star formation rate, entailing a stronger UV field within the cloud. In fact, the SFR in the two GMCs differs by a factor ≈30× ($\mathrm{SFR}^{\rm hi\text{-}z} = 4.8\times10^{-3}$ $\mathrm{M_\odot\,yr^{-1}}$ versus $\mathrm{SFR}^{\rm MW} = 1.5\times10^{-4}$ $\mathrm{M_\odot yr^{-1}}$). Note that the different $T_{\rm d}$ shifts the emission peak from 100 μm (MW) to ∼47 μm at high-z.

Moreover, we fit the above IR spectra to compare the recovered temperature with the luminosity-weighted dust temperature from the model. As discussed in Section 1, the two should correspond. Nevertheless, this sanity check is important since dust temperature in our model has a distribution depending on the grain size and position within the GMC. In the fitting procedure, we use a single-temperature grey body function $B_\lambda(T_{\rm d})k_\lambda$, with k_λ as in equation (22). We leave $\beta_{\rm d}$ and $T_{\rm d}$ as free parameters (in the range $1.5 < \beta_{\rm d} < 2.5$, and $10\,{\rm K} \leq T_{\rm d} \leq 70\,{\rm K}$). The recovered temperatures are consistent with $\langle T_{\rm d}\rangle_{\rm L}$ for both the MW and high-z cloud:

$$T_{\rm d,fit}^{\rm MW} = 19\pm1\ {\rm K} \quad T_{\rm d,fit}^{\rm hi-z} = 40\pm2\ {\rm K} \tag{27a}$$

where the corresponding values for the luminosity-weighted temperatures are

$$\langle T_{\rm d}\rangle_{\rm L}^{\rm MW} = 19\ {\rm K} \quad \langle T_{\rm d}\rangle_{\rm L}^{\rm hi\text{-}z} = 37\ {\rm K} \tag{27b}$$

We have repeated the fitting procedure also for the high-z cloud at 10 Myr of stellar age: we find $T_{\rm d,fit}^{\rm hi\text{-}z} = 62\pm3$ K, consistent with our $\langle T_{\rm d}\rangle_{\rm L}^{\rm hi\text{-}z} = 60$ K. This is particularly interesting and useful, as $T_{\rm d,fit}$ represents the temperature generally used for extrapolating IR luminosity.

Another quantity of interest that can be deduced from our model is the FIR luminosity per unit mass of gas in the GMC. We integrate the FIR luminosity over wavelength and divide by the mass of the cloud, and for the high-z GMC at the end of its lifetime (10.4 Myr) we find

$$\frac{L_{\rm FIR}}{M} \sim 10\,\mathrm{L_\odot/M_\odot}\,. \tag{28a}$$

This value exceeds by ∼10× the one we find in our MW cloud, where we have at the end of its lifetime (2.3 Myr):

$$L_{\rm FIR}/M \sim 1\,\mathrm{L_\odot/M_\odot}\,. \tag{28b}$$

This value is consistent with the average value observed in MW GMCs in which the H II region is obscured (Scoville & Good 1989).

As a caveat, we warn that so far we have discussed the intrinsic luminosity of our clouds. In order to compute the observed luminosity, one would need to account for the fact that dust emission is observed against the CMB; hence, the latter must be subtracted out (as in Ferrara et al. 2017). However, as $\langle T_{\rm d}\rangle_{\rm L} \gg T_{\rm CMB}$ in our clouds, such correction is negligible, as it can be realized from an inspection of Fig. 5 where the dust and CMB spectra are compared.

Our results show a colder mass-weighted, but consistent luminosity-weighted dust temperature with respect to simulations by Liang et al. (2019) (see Section 1). We also confirm that mass-weighted dust temperatures are in general significantly lower than luminosity-weighted ones. Indeed, at redshift $z = 6$ they find that the bulk of the dust mass is as cold as $\langle T_{\rm d}\rangle_{\rm M} = 30.7$ K, while from SED fitting they find the equivalent temperature to be around $T_{\rm d,eqv} \sim$ 45–50 K. These modest quantitative differences are not surprising as in this work they are considering very compact systems, optically thick to IR, which is not the case of our clouds (see discussion at the end of Section 5.1). Moreover our GMCs are not exposed to an external radiation field, thus approaching the surface dust

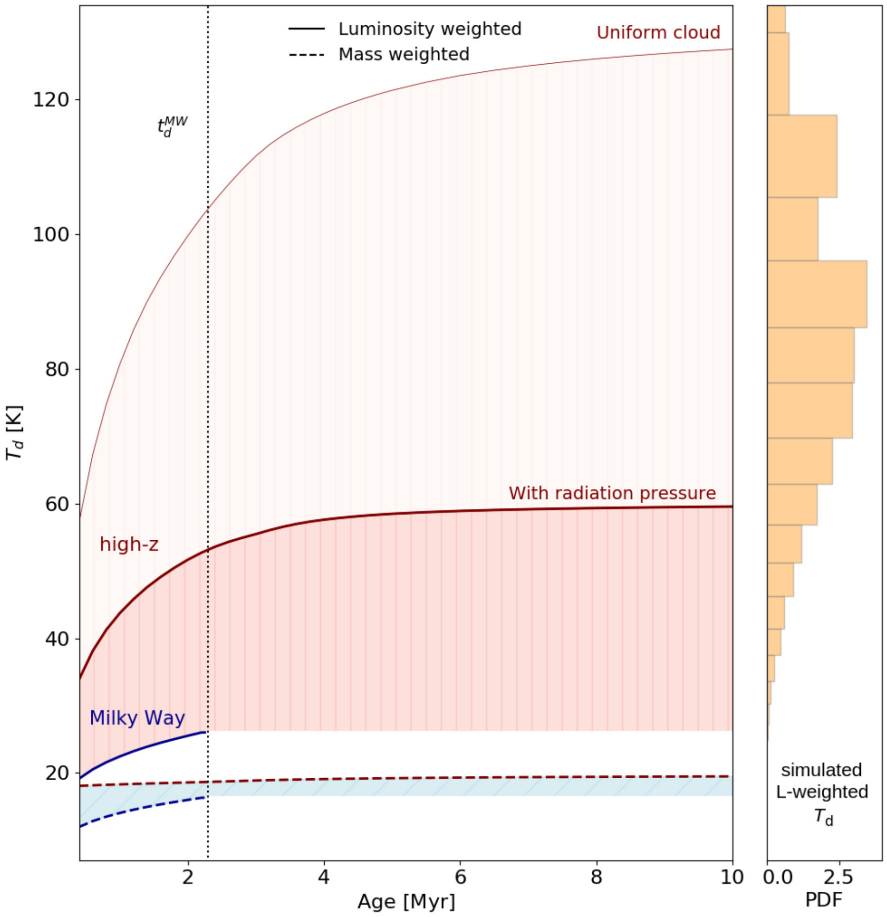

Figure 4. Mass-weighted $\langle T_d \rangle_M$ (dashed line) and luminosity-weighted $\langle T_d \rangle_L$ (solid line) dust temperatures at various ages of the cluster and hosting GMC (see Section 5.2.1). The blue line corresponds to the MW cloud, while the brown one to the high-z cloud, already described in Fig. 1. For the thick lines, we always consider the effect of radiation pressure, and we account for the stellar emission evolution until the dispersal of the clouds, which happens at different times in the two cases (see Section 3.1). The thin brown line corresponds to the uniform high-z cloud case, instead. The grey dotted line represents the dispersal time of the MW cloud. The vertical panel shows the normalized distribution of the luminosity weighted dust temperatures in the simulations by Behrens et al. (2018).

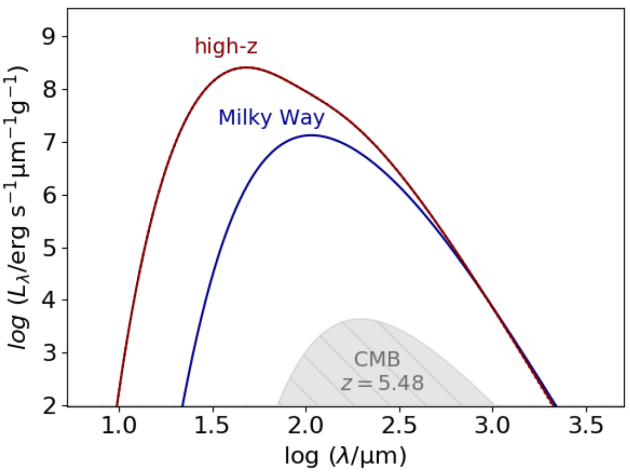

Figure 5. Specific luminosity per unit wavelength of the high-z cloud (brown line) and MW cloud (blue line) at the stellar age of 0.4 Myr. We also show as a comparison the CMB specific luminosity at redshift $z = 5.48$ (grey line). The latter is important because at such redshift, dust emission is observed against it, hence the intensity of the CMB must be subtracted out.

temperature reaches the CMB temperature (and also $\langle T_d \rangle_M \sim T_{CMB}$). Nevertheless, this sort of bi-modality in the dust temperature (see description in Section 1) is in accord with the results of our model (see Fig. 4), and we find a physical motivation for this behaviour as extensively described in Section 5.2.1.

The dust temperature distribution that we infer within our high-z GMC, is also consistent with the findings by Arata et al. (2019). At redshift $z \sim 6$, they find that in the outer low-density regions of their simulated galaxies, a large amount of dust is in thermal equilibrium with the CMB. Instead, for more centrally concentrated dust the temperature increases up to ∼100 K due to a stronger UV flux.

We conclude this Section by comparing our results also with the simulations by Behrens et al. (2018), where the average $\langle T_d \rangle_L = 91 \pm 23$ K at $z = 8.38$ (c.f.r. Laporte et al. 2017). We underline that, even at the remarkably high resolution (≈30 pc) of their simulations, dust temperature effects related to the radiation pressure in H II regions included here, cannot yet be properly treated (see also discussion in Decataldo et al. 2019; Pallottini et al. 2019). This explains the hotter dust temperatures found in their simulations, which lie in between the two curves corresponding to the two models (homogeneous and with a density profile due to radiation pressure, see vertical panel in Fig. 4).

In conclusion, all our results indicate that the dust temperature increases with redshift. This is confirmed also by recent observations (see e.g. Laporte et al. 2019; Bakx et al. 2020). This evidence is not accounted in most observations, which usually assume $T_{\rm d} = 35$–45 K at $z > 5$. This conclusion bears important implications that we are going to discuss next.

7 IMPLICATIONS

The conclusion reached so far, namely that dust is on average warmer at early cosmic times, entails a number of important implications that we briefly discuss here.

7.1 Obscured UV emission

At redshift $5 \leq z \leq 10$ the star formation rate density (SFRD) is usually probed in the rest-frame UV (e.g. Finkelstein et al. 2012; Oesch et al. 2012; Bouwens et al. 2016), but at the moment there is no consensus on the obscured fraction of UV emission at these early epochs. Clearly, not taking into account obscuration, can lead to underestimate the star formation rate in early structures. Interestingly, we find that UV photons emitted by newly born stars are completely absorbed within our high-z GMCs up to the time of dispersal, $t_{\rm d}$, when the gas is removed by stellar feedback. This feature is not appreciably modified by the inclusion of radiation pressure and the subsequent formation of a low-density cavity in the central regions of the GMC. Hence, the unobscured UV emission observed in high-z galaxies should come from clouds that have already been dispersed (see Section 3.1), either due to mechanical or radiative processes (Section 4). In short, the obscured fraction depends on cloud lifetimes.

To get a rough estimate of the fraction of obscured UV emission within our typical high-z GMC, we integrate the UV luminosity at 1500 Å for continuous star formation until $t_{\rm d}$.[10] After the cloud is dispersed, all the UV photons leaks away. We can then compute the ratio between obscured UV photons (those produced before $t_{\rm d}$) and all the produced UV photons:

$$f_{\rm UV,obscured} = \frac{\int_0^{t_{\rm d,Myr}} L_{1500\text{Å}}(t)\,{\rm d}t}{\int_0^{100\rm Myr} L_{1500\text{Å}}(t)\,{\rm d}t}, \tag{29}$$

where the upper limit of 100 Myr is indicative of the time at which the UV emission from the past star formation episodes becomes negligible. We find that $f_{\rm UV,obscured} \simeq 0.42$, i.e. almost half of the energy in the UV produced by star formation in our high-z GMC is obscured. Note that in our MW cloud this fraction is much lower, around $f_{\rm UV,obscured} \simeq 0.18$, basically due to the shorter lifetime of the cloud. Our finding is consistent with recent high-z observations.

So far, dust obscuration has been observed at $z \sim 7$ by Bowler et al. (2018) in six bright LBGs. They were able to obtain a $5\,\sigma$ detection of the highest redshift galaxy targeted, but no detection of the five remaining sources. From a stacking analysis they determined the average FIR luminosity of the sample to be $L_{\rm FIR} \sim 2 \times 10^{11}\,{\rm L}_\odot$. Then, converting this observed FIR luminosity into a star formation rate, they found that ≈ 50 per cent of the total SFR is obscured by dust. Moreover, Fudamoto et al. (2020) recently observed that within their UV-selected sample, massive galaxies [$\log(M_*/{\rm M}_\odot) > 10$] at $z \sim 5$–6 exhibit an obscured fraction of star formation of ~ 45 per cent. All together these results indicate a rapid build-up of dust during the EoR.

[10] In practice, we approximate the continuous SFR with a series of subsequent bursts, and the resulting $f_{\rm UV,obscured}$ converges considering more than 20 bursts.

7.2 IRX–β relation

In Section 1, we introduced the empirical IRX–β relation, that is used to correct for dust obscuration in UV-selected galaxies at $z > 5$. This relation is confirmed to hold up to $z \sim 2$–3, but it is yet unclear whether it applies at higher redshift where a large scatter is present in the data (Barisic et al. 2017; Fudamoto et al. 2017). On average, high-z galaxies are shown to have low IRX, and lie below the local relation (Capak et al. 2015; Bouwens et al. 2016). However, as discussed in Section 1, this conclusion is heavily dependent on the dust temperature assumption for the SEDs of dust emission, which is generally set in $T_{\rm d} = 35$–45 K. This might lead to a severe underestimate of the high-z galaxies FIR luminosity (see the re-analysis of the sample by Capak et al. 2015 performed by Barisic et al. 2017)

As already pointed out by Bouwens et al. (2016), the tension with the local relation would be alleviated by warmer dust, with $T_{\rm d} = 45$–50 K. In addition, even if the bulk of the dust remained cold ($\sim$35 K), a moderate fraction of warm dust is already sufficient to affect the SEDs (see the discussion in Section 5.2.1), reducing the apparent flux on the Rayleigh–Jeans tail at fixed $L_{\rm FIR}$ (Casey et al. 2018). This scenario is consistent with our conclusion on dust temperature in high-z GMCs, where due to the large turbulent velocities and consequent high SFR, dust attains temperatures as high as $T_{\rm d} \simeq 60$ K. The resulting increase in FIR luminosity, and consequently in IRX parameter, is as large as 1.4 dex (computed using equation 25) with respect to considering $T_{\rm d} = 35$ K. This is sufficient to shift the IRX faint galaxies back on the local relation. As a final remark, we notice that IRX–β relation implicitly assumes that FIR and UV emitting regions are co-spatial. However, if dust completely absorbs the radiation emitted by stars within GMCs, as suggested here, FIR and UV emitting regions might actually be spatially segregated (Behrens et al. 2018).

7.3 Dust mass estimates from $L_{\rm FIR}$

Higher dust temperatures imply that a smaller dust amount can produce the same FIR luminosity, see equation (25). This would alleviate the problem of a superefficient dust production by stellar sources that is very hard to reconcile with available data and theoretical results; see discussion in e.g. Tamura et al. (2019) for the galaxy MACS0416Y1 at $z = 8.31$ (whose 90 μm continuum is observed).

For instance given $L_{\rm FIR}$, assuming $T_{\rm d} = 60$ K, which is the maximum value derived for our high-z GMC (when the radiation pressure effect is included), would result in a dust mass reduction by a factor $\Delta M_{\rm d} = (50/60)^{4+\beta_{\rm d}} = 0.33$ with respect to the value suggested by Tamura et al. (2019) who took $T_{\rm d} = 50$ K. The power $4 + \beta_{\rm d} = 6$ is derived from the integration of the greybody function (equation 25).This result is shown graphically in Fig. 6, where we compare the dust mass estimates for MACS0416Y1 resulting from three different assumptions for the dust temperature, $T_{\rm d} = (40, 50, 60)$ K.

We can also compute the dust mass per SN event produced for these three cases, by using the stellar mass computed by Tamura et al. (2019), $M_* \sim 2 \times 10^8\,{\rm M}_\odot$:

$$\text{dust yield per SN} = \frac{M_{\rm d}}{M_* \nu_{\rm SN}}, \tag{30}$$

where $\nu_{\rm SN}$ (see equation 11) is the number of SNe per solar mass of stars formed. We obtain that for $T_{\rm d} = 50$ K, which is the most

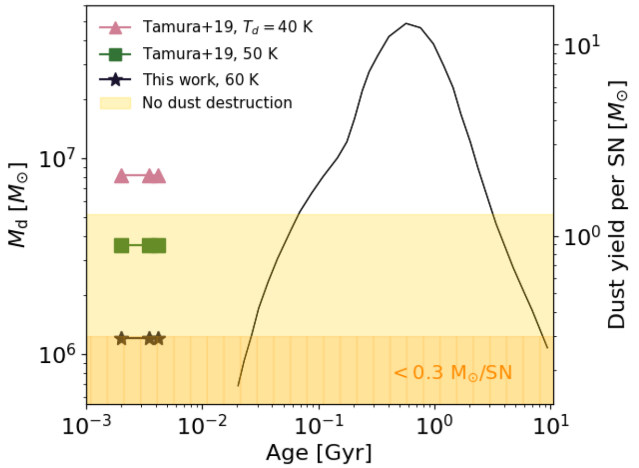

Figure 6. Time evolution of dust mass predicted in a dust formation model (e.g. Asano et al. 2013; Nozawa et al. 2014) as a function of galaxy age with an initial gas mass of $M_{\rm gas} = 2 \times 10^{10}\,{\rm M}_\odot$ and a star formation time scale of $\tau_{\rm SFH} = 0.3$ Gyr. This plot is adapted from Tamura et al. (2019, fig. 6, lower right panel). The symbols correspond to the best-fitting parameters of the physical properties of MACS0416Y1 ($z = 8.31$) estimated through Calzetti et al. (2000), MW, and SMC extinction laws (from right to left). Each colour and shape corresponds to a different assumption for the dust temperature $T_{\rm d}$, as shown by the legend. On the left y-axis we also show which would be the dust yield per SN event depending on the computed dust mass, and so on the assumed dust temperature (see text). The yellow shaded region corresponds to the maximum theoretical dust yield without dust destruction in SNe explosions, and the hatched orange region to the upper limit assuming $T_{\rm d} = 60$ K.

optimistic case considered by Tamura et al. (2019), around $\sim$1 $M_\odot$ of dust should be produced in each SNe explosion. This value exceeds the most recent constraints on SN dust yields by Leśniewska & Michałowski (2019) when we allow for some dust destruction during SNe explosions. Moreover, for the most frequently assumed value of the dust temperature $T_{\rm d} = 40$ K, we get 2 $M_\odot$ of dust yield per SN event, which exceeds even the less stringent constraints available (i.e. with no dust destruction, see the yellow shaded region in Fig. 6). Instead, if we consider $T_{\rm d} = 60$ K, dust yield drops to a modest 0.3 $M_\odot$, a value more in line with current data.

We also note that recent observations of MACS0416Y1, indicate the presence of warmer dust in this galaxy. Bakx et al. (2020) fail to detect continuum emission at 160 μm (rest frame) down to 18 μJy. This non-detection places strong limits on the dust spectrum, given the observed continuum emission at longer wavelengths 850 μm (Tamura et al. 2019). In particular, it suggests an unusually warm dust component $T_{\rm d,L} > 80$ K (90 per cent confidence limit) considering an emissivity index $\beta_{\rm d} = 2$. This would further decreases the required dust masses, with a reduction factor of 0.06 with respect to the value deduced by Tamura et al. (2019).

8 SUMMARY

In this work, we have developed a detailed model for dust temperature and associated far infrared (FIR) emission within star-forming GMCs. We emphasize the difference between local and high-z GMCs, which is connected mainly to the larger pressure (p) and the turbulent velocity (σ) within early galaxies. These differences have two crucial effects: the star formation rate, which we showed to depend only on σ^3, is $\sim$30 times larger in high-z clouds, and the optical depth to ultra violet (UV) is $\sim$10 times higher due to the increase in the cloud column density, which depends on $p^{1/2}$. We have also analysed the effects of UV radiation for the formation of H II regions and radiation pressure – in short radiative feedback – which, along with mechanical feedback from stellar winds and SNe, determine the cloud dispersal time-scale.

Our main findings are summarized as follows:

(i) **Dust temperature in star-forming GMCs**: In high-z clouds dust is warmer than in local ones, reaching $T_{\rm d} = 60$ K. This results from (i) the more compact structure of GMCs, and (ii) the more turbulent nature of early galaxies;

(ii) **Clouds lifetimes**: Star formation (and associated UV emission) is heavily obscured within the very compact high-z clouds. Due to their compact nature, these structures also survive longer (about $\sim$4×) than local clouds to H II region expansion, stellar winds and SNe. Their lifetimes are $\sim$10 Myr.

(iii) **Infrared emission from star forming GMCs**: High-z clouds are intense FIR emitters, with a luminosity-to-gas mass ratio of $\sim$10 $L_\odot/M_\odot$, which is 10 times higher than the value of our reference MW cloud.

These results have some very significant implications. The unobscured UV emission observed in high-z galaxies mainly comes from clouds that have already been dispersed, and hence depends on cloud lifetimes. This may lead to a spatial separation between the UV, which arises from the diffuse ISM, and the FIR emission, associated with compact clouds. Our scenario seems to be supported by simulations (Behrens et al. 2018) and observations (e.g. Laporte et al. 2017; Bowler et al. 2018), which find a significant spatial offset between ALMA and *HST* data. The spatial offset between UV and FIR might lead to questioning the significance of the IRX–β relation at high redshift. In any case, the higher dust temperatures predicted here, would reduce the tension between local and high-z IRX–β relation, shifting the early IRX faint galaxies back on the local relation. Warmer dust also reduces the problem of insufficient dust production due to star formation in early times (<0.1 Gyr). Indeed, the dust yield produced per SN event within our clouds is in agreement with the most updated SN efficiency constraints.

Finally, warmer dust produces a strong interstellar FIR radiation field pervading the galaxy, and hence GMCs. This 'background' might affect FIR emission lines, such as the fine-structure [C II] 158 μm line in two ways by (1) altering the population levels of C^+, and (2) decreasing the line-to-continuum contrast of [C II]. These two effects might possibly be responsible for the observed [C II] deficit in luminous FIR emitting galaxies ($L_{\rm FIR} > 10^{11}\,{\rm L}_\odot$). In addition it could induce significant spatial variations in the [C II]/FIR ratio as hinted by recent observations of high-z starbursts (e.g. Oteo et al. 2016).

Given the relevant implications that warm/hot dust may have for galaxy formation at early epochs, it is of utmost importance to measure dust temperature in high-z galaxies. This will become possible in the near future by means of planned infrared observatories such as SPICA (e.g. Spinoglio et al. 2017; Egami et al. 2018).

ACKNOWLEDGEMENTS

LS, AF, SC, and DD acknowledge support from the ERC Advanced Grant INTERSTELLAR H2020/740120. Any dissemination of results must indicate that it reflects only the author's view and that the Commission is not responsible for any use that may be made of the information it contains. Partial support (AF) from the Carl Friedrich von Siemens-Forschungspreis der Alexander von Humboldt-Stiftung Research Award is kindly acknowledged. We thank Rebecca Bowler, Alessandro Lupi, and Pascal Oesch for useful discussions. We acknowledge use of the PYTHON programming language (Van Rossum & de Boer 1991), MATPLOTLIB (Hunter

2007), NUMPY (van der Walt, Colbert & Varoquaux 2011), and SCIPY (Virtanen et al. 2019).

DATA AVAILABILITY

Part of the data underlying this article were accessed from the computational resources available to the Cosmology Group at Scuola Normale Superiore, Pisa (IT). The derived data generated in this research will be shared on reasonable request to the corresponding author.

REFERENCES

Arata S., Yajima H., Nagamine K., Li Y., Khochfar S., 2019, MNRAS, 488, 2629
Asano R. S., Takeuchi T. T., Hirashita H., Nozawa T., 2013, MNRAS, 432, 637
Baes M. et al., 2003, MNRAS, 343, 1081
Baes M., Verstappen J., Looze I. D., Fritz J., Saftly W., Pérez E. V., Stalevski M., Valcke S., 2011, ApJS, 196, 22
Bakx T. J. L. C. et al., 2020, MNRAS, 493, 4294
Barisic I. et al., 2017, ApJ, 845, 41
Behrens C., Pallottini A., Ferrara A., Gallerani S., Vallini L., 2018, MNRAS, 477, 552
Benincasa S. M. et al., 2019, preprint (arXiv:1911.05251)
Bianchi S., 2008, A&A, 490, 461
Bouwens R. J. et al., 2016, ApJ, 833, 72
Bowler R. A. A., Bourne N., Dunlop J. S., McLure R. J., McLeod D. J., 2018, MNRAS, 481, 1631
Buat V., Xu C., 1996, A&A, 306, 61
Calzetti D., 1997, AJ, 113, 162
Calzetti D., Kinney A. L., Storchi-Bergmann T., 1994, ApJ, 429, 582
Calzetti D., Armus L., Bohlin R. C., Kinney A. L., Koornneef J., Storchi-Bergmann T., 2000, ApJ, 533, 682
Capak P. et al., 2011, ApJ, 730, 68
Capak P. et al., 2015, Nature, 522, 455
Casey C. M., 2012, MNRAS, 425, 3094
Casey C. M., Narayanan D., Cooray A., 2014a, Phys. Rep., 541, 45
Casey C. M. et al., 2014b, ApJ, 796, 95
Casey C. M., Hodge J., Zavala J. A., Spilker J., da Cunha E., Staguhn J., Finkelstein S. L., Drew P., 2018, ApJ, 862, 78
Ceverino D., Glover S. C. O., Klessen R. S., 2017, MNRAS, 470, 2791
Conley A. et al., 2011, ApJ, 732, L35
da Cunha E. et al., 2013, ApJ, 766, 13
da Cunha E. et al., 2015, ApJ, 806, 110
Dayal P., Hirashita H., Ferrara A., 2010, MNRAS, 403, 620
Decataldo D., Pallottini A., Ferrara A., Vallini L., Gallerani S., 2019, MNRAS, 487, 3377
Désert F. X. et al., 2008, A&A, 481, 411
Draine B., 2003, ARA&A, 41, 241
Draine B. T., 2004, The Cold Universe. Springer, p. 213
Draine B. T., 2011, ApJ, 732, 100
Draine B. T., Li A., 2001, ApJ, 551, 807
Draine B. T., Li A., 2007, ApJ, 657, 810
Dunne L., Eales S., Edmunds M., Ivison R., Alexander P., Clements D. L., 2000, MNRAS, 315, 115
Dupac X. et al., 2003, A&A, 404, L11
Dyson J., Williams D., 1980, The Physics of the Interstellar Medium, Manchester Univ. Press. Manchester
Egami E. et al., 2018, PASA, 35
Faisst A. L. et al., 2017, ApJ, 847, 21
Faisst A. L., Fudamoto Y., Oesch P. A., Scoville N., Riechers D. A., Pavesi R., Capak P., 2020, preprint (arXiv:2005.07716)
Ferrara A., Tolstoy E., 2000, MNRAS, 313, 291
Ferrara A., Hirashita H., Ouchi M., Fujimoto S., 2017, MNRAS, 471, 5018
Finkelstein S. L. et al., 2012, ApJ, 756, 164
Fudamoto Y. et al., 2017, MNRAS, 472, 483
Fudamoto Y. et al., 2020, preprint (arXiv:2004.10760)
Gallerani S. et al., 2010, A&A, 523, A85
Genzel R. et al., 2017, Nature, 543, 397
Glazebrook K., 2009, Nature, 460, 694
González-López J. et al., 2014, ApJ, 784, 99
Gordon K. D., Misselt K. A., Witt A. N., Clayton G. C., 2001, ApJ, 551, 269
Grisdale K., Agertz O., Renaud F., Romeo A. B., 2018, MNRAS, 479, 3167
Guhathakurta P., Draine B. T., 1989, ApJ, 345, 230
Heyer M., Krawczyk C., Duval J., Jackson J. M., 2009, ApJ, 699, 1092
Hildebrand R. H., 1983, QJRAS, 24, 267
Hopkins P. F. et al., 2018, MNRAS, 480, 800
Hunter J. D., 2007, Comput. Sci. Eng., 9, 90
Kennicutt R. C., Jr et al., 1998, ApJ, 498, 181
Kirkpatrick A., Pope A., Sajina A., Roebuck E., Yan L., Armus L., Díaz-Santos T., Stierwalt S., 2015, ApJ, 814, 9
Kriek M., Conroy C., 2013, ApJ, 775, L16
Krumholz M. R., Tan J. C., 2007, ApJ, 654, 304
Laporte N. et al., 2017, ApJ, 837, L21
Laporte N. et al., 2019, MNRAS, 487, L81
Larson R. B., 1981, MNRAS, 194, 809
Leitherer C. et al., 1999, ApJS, 123, 3
Leśniewska A., Michałowski M. J., 2019, A&A, 624, L13
Leung T. K. D., Pallottini A., Ferrara A., Mac Low M.-M., 2019, preprint (arXiv:1907.02972)
Liang L., et al., 489, 2019, MNRAS, 1397
Licquia T. C., Newman J. A., 2015, ApJ, 806, 96
Lupi A., Bovino S., Capelo P. R., Volonteri M., Silk J., 2018, MNRAS, 474, 2884
Ma X. et al., 2019, MNRAS, 487, 1844
Meurer G. R., Heckman T. M., Calzetti D., 1999, ApJ, 521, 64
Nozawa T., Asano R. S., Hirashita H., Takeuchi T. T., 2014, MNRAS, 447, L16
Oesch P. et al., 2012, ApJ, 759, 135
Oteo I. et al., 2016, ApJ, 827, 34
Pallottini A., Ferrara A., Gallerani S., Vallini L., Maiolino R., Salvadori S., 2017a, MNRAS, 465, 2540
Pallottini A., Ferrara A., Bovino S., Vallini L., Gallerani S., Maiolino R., Salvadori S., 2017b, MNRAS, 471, 4128
Pallottini A. et al., 2019, MNRAS, 487, 1689
Paradis D., Bernard J. P., Mény C., 2009, A&A, 506, 745
Paradis D. et al., 2010, A&A, 520, L8
Planck Collaboration XIX, 2011a, A&A, 536, A19
Planck Collaboration XXV, 2011b, A&A, 536, A25
Popping G., Puglisi A., Norman C. A., 2017, MNRAS, 472, 2315
Raga A., Cantó J., Rodríguez L., 2012, MNRAS, 419, L39
Riechers D. A. et al., 2013, Nature, 496, 329
Rosdahl J. et al., 2018, MNRAS, 479, 994
Rosolowsky E., Blitz L., 2005, ApJ, 623, 826
Schaerer D., de Koter A., 1997, A&A, 322, 598
Schaerer D., Charbonnel C., Meynet G., Maeder A., Schaller G., 1993, A&AS, 102, 339
Schmidt M., 1959, ApJ, 129, 243
Scoville N. Z., Good J. C., 1989, ApJ, 339, 149
Semenov V. A., Kravtsov A. V., Gnedin N. Y., 2018, ApJ, 861, 4
Shibuya T. et al., 2014, ApJ, 788, 74
Spinoglio L. et al., 2017, PASA, 34, e057
Stratta G., Gallerani S., Maiolino R., 2011, A&A, 532, A45
Tamura Y. et al., 2019, ApJ, 874, 27
Vallini L., Pallottini A., Ferrara A., Gallerani S., Sobacchi E., Behrens C., 2018, MNRAS, 473, 271
van der Walt S., Colbert S. C., Varoquaux G., 2011, Comput. Sci. Eng., 13, 22
Van Rossum G., de Boer J., 1991, CWI Q., 4, 283
Virtanen P. et al., 2019, preprint (arXiv:1907.10121)
Walcher J., Groves B., Budavári T., Dale D., 2011, Ap&SS, 331, 1
Weingartner J. C., Draine B., 2001, ApJ, 548, 296
Weiß A. et al., 2013, ApJ, 767, 88
Willott C. J., Carilli C. L., Wagg J., Wang R., 2015, ApJ, 807, 180
Xue X. X. et al., 2008, ApJ, 684, 1143

This paper has been typeset from a TEX/LATEX file prepared by the author.